7-2008

Observations of neutral depletion and plasma acceleration in a flowing high-power argon helicon plasma

C. Mark Denning

Matt Wiebold
College of Saint Benedict/Saint John's University, mwiebold@csbsju.edu

John E. Scharer

Recommended Citation

Denning CM, Wiebold M, Scharer JE. 2008. Observations of neutral depletion and plasma acceleration in a flowing high-power argon helicon plasma. *Physics of Plasmas* 15(7): 072115.

Observations of neutral depletion and plasma acceleration in a flowing high-power argon helicon plasma

C. Mark Denning, Matt Wiebold, and John E. Scharer
Electrical and Computer Engineering Department, University of Wisconsin-Madison, Engineering Research Building, 1500 Engineering Dr., Madison, Wisconsin 53704, USA

(Received 17 April 2008; accepted 23 May 2008; published online 22 July 2008)

Neutral depletion effects are observed in a steady-state flowing argon helicon plasma with a magnetic nozzle for high rf input powers (up to 3 kW). Noninvasive diagnostics including 105 GHz microwave interferometry and optical spectroscopy with collisional-radiative modeling are used to measure the electron density (n_e), electron temperature (T_e), and neutral density (n_n). A region of weak neutral depletion is observed upstream of the antenna where increasing rf power leads to increased electron density (up to $n_e = 1.6 \times 10^{13}$ cm^{-3}) while T_e remains essentially constant and low (1.7–2.0 eV). The downstream region exhibits profound neutral depletion (maximum 92% line-averaged ionization), where T_e rises linearly with increasing rf power (up to 4.9 eV) and n_e remains constrained (below 6.5×10^{12} cm^{-3}). Flux considerations indicate accelerated plasma flow (Mach 0.24) through the antenna region due to an axial pressure gradient with reduced collisional drag from neutral depletion. © *2008 American Institute of Physics*. [DOI: 10.1063/1.2950301]

I. INTRODUCTION

The role of neutrals in highly ionized, low-temperature laboratory plasmas remains an important question. The reduction in the neutral density as a result of ionization can have significant effects on the properties of a plasma. A number of experiments that demonstrate various effects of neutral depletion have been performed in recent years. Boswell first considered neutral depletion in helicon plasmas, observing a fully ionized core plasma in argon, attributing neutral depletion to neutral gas heating and rarefaction.[1] Direct measurements of neutral pressure with probes along the axis of an argon helicon plasma showed significant neutral depletion in the center of the discharge.[2] Similar results were observed radially in an inductively coupled magnetized wafer processing discharge.[3] Miljak *et al.* observed a density maximum in a high-power, double-antenna helicon discharge attributed to neutral depletion.[4] Oscillations in plasma density have been observed due to competing effects of neutral loss through ionization and refilling of neutrals from a diffusion chamber.[5] Recent experiments have involved direct measurements of neutral density using spectroscopic techniques, such as, a collisional-radiative model in argon helicon plasmas,[6] two-photon laser-induced fluorescence (LIF) measurements of neutral xenon density,[7] and neutral density measurements from neutral pressure and rotational temperature measurements in a nitrogen processing discharge.[8] Additionally, computational simulations have been performed to model neutral transport and depletion.[9–11] Theoretical formulations have also been developed to address the effect of neutral depletion in pulsed helicon discharges[12] and power and particle balance coupling arising from depletion.[13,14]

Our research group has previously investigated helicon wave propagation and plasma density in nonuniform magnetic fields, as well as electron temperature anisotropy[15] and computational wave simulation agreement with experimental observations.[16] The current work extends our previous research to higher rf power levels (up to 3 kW) and lower pressure regimes (as low as 0.4 mTorr), includes magnetic nozzle effects, and incorporates new spectroscopic diagnostics to investigate the effects of neutral depletion. With microwave interferometry and spectroscopic techniques that incorporate collisional-radiative (CR) models for both Ar I (Ref. 17) and Ar II (Ref. 18) we have measured the electron density (n_e), neutral density (n_n), and electron temperature (T_e) as a function of input rf power, argon gas flow rate, magnetic field strength, and axial position. These diagnostics have provided new insight into the fundamental operation of high-power helicon sources. We have observed a region of low neutral depletion [less than 30% fractional ionization, defined as $n_e/(n_e+n_n)$] upstream of the antenna where the plasma is collisional with the neutral gas and n_e increases with rising rf power while T_e remains essentially constant. A flat axial pressure profile is observed in this region due to balance between the neutral pressure at the upstream edge of the discharge and the plasma source pressure. In contrast, the region downstream of the antenna exhibits high neutral depletion (more than 80% fractional ionization). Here neutral collisions are negligible and n_e saturates as the rf input power is increased, and in many cases even decreases as the power is increased. In this highly depleted collisionless region, T_e increases monotonically with rising rf power, and a pressure gradient is observed between the source region and the turbopump downstream. Evidence of an accelerated plasma flow in the downstream region is seen that is directly proportional to rf power and the level of neutral depletion. Magnetic nozzle effects on the plasma density downstream of the antenna source region are also observed.

Neutral depletion is expected to affect the formation of a double layer in the downstream expanding magnetic field, because it can lead to both high electron temperatures that affect the associated potential drop and a lower neutral density that reduces ion-neutral collisions which impede ion ac-

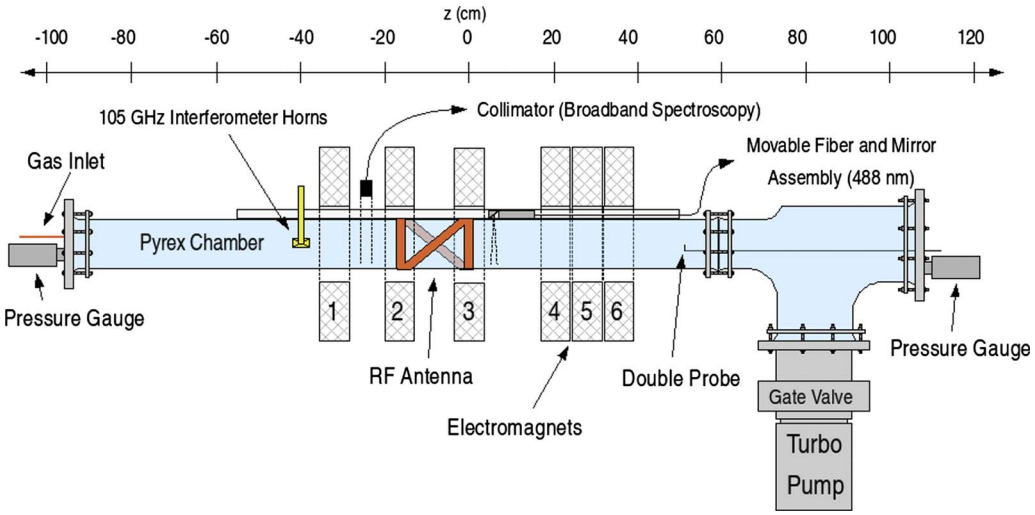

FIG. 1. (Color online) Experimental apparatus.

celeration and double layer formation.[19] The substantial, though subsonic, velocity with which the ions and electrons enter the double layer region will also play a role. Additionally, these findings will be of interest for research being performed on plasma thrusters with magnetic nozzles, for which plasma production efficiency and particle dynamics are of great importance.

This paper is organized as follows: the experimental setup and diagnostics are described in Sec. II, the experimental results are presented in Sec. III, discussion and analysis appears in Sec. IV, with concluding remarks in Sec. V.

II. EXPERIMENTAL APPARATUS

A. Helicon plasma source

The current apparatus (Fig. 1) is an upgrade of the experiment described in a previous work.[16] The vacuum chamber consists of a 10-cm-inner-diameter Pyrex tube (1.5 m long) and tee section (46 cm long) terminated by grounded aluminum plates on both ends, located at $z=-91$ cm and 105 cm, where $z=0$ is the downstream edge of the antenna and the positive-z direction points in the direction of gas flow. A 5-mm-inner-diameter line supplies gas to the chamber at the upstream plate, while the downstream plate has a probe feedthrough (3.5 cm off-axis). The tee section is connected to a Varian turbomolecular pump that provides a base pressure of 1×10^{-6} Torr. The volumetric argon gas flow rate in standard cubic centimeters per minute (sccm) is measured using a McMillan 50SD-6 mass flow meter, and the fill pressure is measured at both the upstream and downstream end plates using two MKS 910 Dual Transducer piezo-based pressure gauges. A series of electromagnets, each 7 cm wide, provides a static magnetic field in either a "flat" or "nozzle" configuration (Fig. 2), with less than 4% variability in the flat region of either field configuration. The configuration can be switched by a small adjustment of the axial position of magnets 4 and 6 and by turning on or off the current in magnet 5. A coil current of up to 180 A provides axial fields as high as 1.04 kG in the flat field region (between magnets 1 and 4) and a 1.5 kG peak field in the nozzle configuration. (The field strengths in this paper refer to the magnitude in the source region, the nozzle peak level being 1.44 times higher.) An 18-cm-long, half-turn double-helix antenna is wrapped around the Pyrex chamber and couples in 13.56 MHz rf power. The antenna is fed through a capacitive matchbox with less than 2% power reflection measured. Two rf power generators are used, a pulsed, broadband Amplifier Research rf amplifier run at 13.56 MHz with a maximum power of 1 kW (6 ms pulses with 16.5 Hz rep rate), and a fixed-frequency (13.56 MHz) cw advanced energy rf source with a maximum power of 3 kW. All of the data except for the plasma density measurement comparison (see Sec. III A) were taken using the 3 kW cw generator to create discharges lasting at least 1.5 s, which is sufficient to reach steady-state plasma production. It is important to note that helicon plasmas at sufficient rf powers and magnetic field strengths exhibit a sharp density jump associated with the so-called "blue

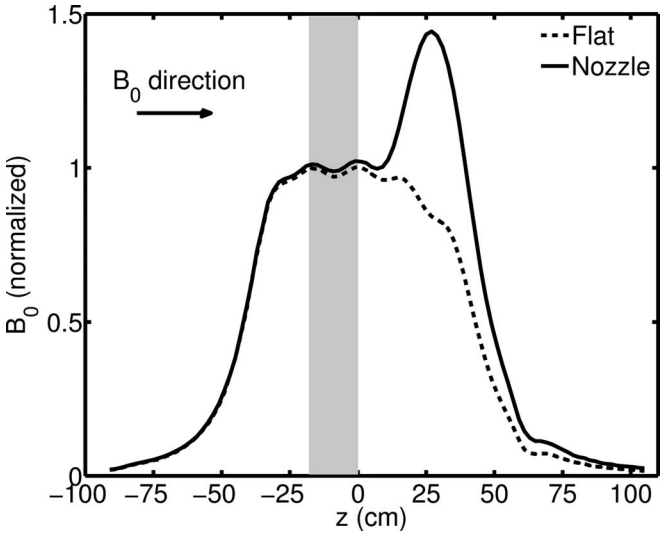

FIG. 2. Static applied magnetic field profiles for the flat (dashed) and nozzle (solid) configurations, normalized to the source region field (maximum 1.04 kG with 1.5 kG peak nozzle field). The shaded region denotes the extent of the rf antenna.

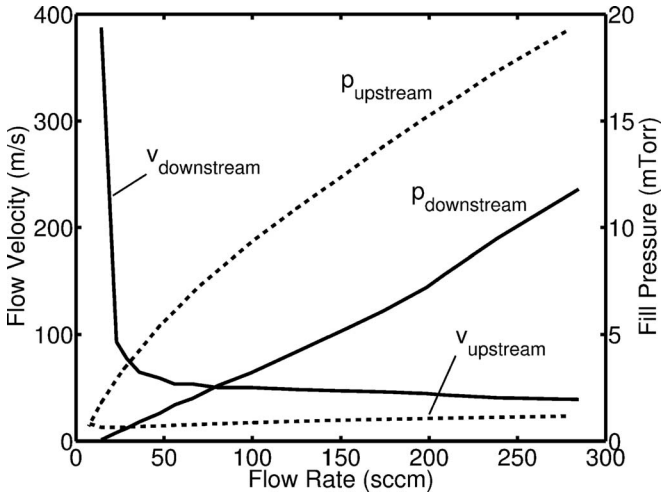

FIG. 3. Measured argon fill gas pressure and calculated flow velocity vs flow rate for upstream (dashed) and downstream (solid) regions.

mode"[16,20] and that all data presented are for blue mode discharges. No rf mode jumps were observed over the range of powers and magnetic field strengths used.

An important difference between our experiment and many previous experiments is that the argon gas is fed in on the upstream side of the chamber and is pulled through the antenna source region by a turbopump on the opposite, downstream side. This is opposed to experiments in which gas is fed in on the pump side of the chamber and must diffuse past the pumping region into the plasma source region. In this way the plasmas discussed here are in a continuously flowing gas configuration, as opposed to a quasistatic scenario in which gas must diffuse into the source region. One consequence of this is that we do not observe oscillations in density as those seen by Degeling *et al.*[5]

The measured fill pressure and calculated gas flow velocity in the 10-cm-diameter chamber are shown in Fig. 3 as a function of flow rate at both the upstream and downstream end plates. The neutral gas flow velocity v_n is determined using $v_n=(Q/A)(p_{\mathrm{atm}}/p_n)$, where Q is the measured volumetric flow rate assuming standard temperature and pressure, A is the cross-sectional area of the chamber, and p_n and p_{atm} are the chamber pressure and standard atmospheric pressure, respectively. The upstream pressure is higher than the downstream pressure at any given flow rate, while the upstream velocity is lower than the downstream velocity. This is a consequence of the gas entering through the inlet and then accelerating and expanding over the length of the plasma chamber. The upstream and downstream pressures were also measured during plasma operation and these data are presented in Sec. III. Because the fill pressure varies significantly along the axis of the experiment, the flow rate is used to uniquely specify the fill condition.

B. Diagnostics

1. Interferometer

A 105 GHz Mach–Zehnder millimeter-wave interferometer is used to determine the electron density (n_e), line-averaged over the 10 cm chamber diameter. This diagnostic has been previously cross-checked by the Langmuir probe[16] and more recently by a double probe (see Sec. III A). Our research group has also used interferometry to diagnose collision frequencies and electron temperatures in high-pressure plasmas.[21] The interferometer wave is perpendicularly polarized to the magnetic field leading to X-mode propagation. However, in the regimes in which the interferometer is operated, the wave propagation is nearly identical to O-mode propagation. The difference in interferometer phase shift between the O- and X-modes is at most 0.1% for the parameters of our experiment. For O-mode propagation, the phase shift varies linearly with the electron density such that $n_e=2.07f\Delta\phi/d$ (cm^{-3}), where f is the interferometer frequency (Hz), d is the chamber diameter (cm), and $\Delta\varphi$ is the phase shift (degrees).[22] Using radial density profiles measured by a Langmuir probe, the peak electron density can be determined. Interferometer measurements in the magnetized source region are only possible where there are sufficient gaps between the electromagnets to position the microwave horns. The nozzle configuration allows measurements between the magnets at $z=-25$ cm and 11 cm, while the flat field configuration allows for downstream measurements at a third position, $z=22$ cm. Unrestricted measurements are possible beyond the magnets, from the upstream end plate at $z=-91$ to -40 cm, and from $z=42$ cm to the downstream end plate at $z=105$ cm. The helical antenna and rf feeds make measurement between magnets 2 and 3 ($z=-18$ to 0 cm) impractical.

2. Double Langmuir probe

A double Langmuir probe is used to measure the ion density and electron temperature[23,24] as a crosscheck for the interferometer and 488 nm emission density diagnostics. The probe consists of two differentially biased thoriated tungsten tips, 0.5 mm in diameter and 0.8 mm in length, separated by 2 mm and pointed perpendicularly to the magnetic field. A section of two-hole alumina tubing insulates the probe tips from one another. The probe is in a dogleg configuration to allow measurement of both axial and radial profiles. Like all current-collecting probes, the double probe is susceptible to rf effects which can affect the slope of the I-V trace leading to erroneous T_e measurements. The ion saturation portion of the curve is far less sensitive to these effects, and is used here, along with T_e determined by a collisional-radiative code, to determine the plasma density for the diagnostic comparison (see Sec. III A). It was also found that the probe experienced significant heating in cw plasma operation. For this reason the double probe is used here exclusively for crosschecking the plasma density from the interferometer and spectroscopic diagnostics at low powers (less than 1 kW) in pulsed discharges for which heat loading is minimal.

3. Optical spectroscopy: Ar II 488 nm

A 45° mirror mounted on an axially movable assembly reflects optical plasma emission into a fiber connected to a 0.5 m focal length monochromator with a photomultiplier tube (PMT) detector. The intensity is determined by analyz-

ing oscilloscope traces of the PMT signal with a photon counting routine. The mirror assembly slides along the top of the Pyrex tube inside the electromagnets allowing measurements at any axial location. The relative plasma density can be measured using the optical emission intensity I at a given wavelength assuming

$$I \propto n_e n_i \overline{\sigma_x v_e} = n_p^2 \overline{\sigma_x v_e}, \tag{1}$$

where n_e and n_i are the electron and ion densities, σ_x is the electron-ion excitation cross section (a function of electron energy) for the excited state of interest, and v_e is the electron velocity.[25] The $\overline{\sigma_x v_e}$ factor is found by integrating the product of the electron energy distribution function (EEDF), assumed to be a Maxwellian, with tabulated excitation cross-section data. The EEDF is a function of T_e so this quantity must be known to derive accurate density profiles. We use the strong 487.99 nm Ar II ion line corresponding to emission resulting from the $4p\ ^2D^0_{5/2} \rightarrow 4s\ ^2P_{3/2}$ transition, using tabulated excitation cross section data for the initial $4p\ ^2D^0_{5/2}$ state.[26] Since the emission is proportional to the product of the electron and ion densities, the 488 nm diagnostic measures the quasineutral plasma density ($n_p \approx n_e \approx n_i$) in contrast to the interferometer which measures the electron density specifically.

4. Optical spectroscopy with collisional-radiative models

T_e and neutral density (n_n) are measured using broadband ion (Ar II) and neutral (Ar I) optical spectra, respectively. These parameters are determined using two different collisional-radiative (CR) models that calculate excited population densities that can be compared to those measured optically. The codes used to implement these models have been written in Octave, an open-source MATLAB-compatible language.

The radiance of each line of interest is measured using an absolutely calibrated Ocean Optics ST2000 spectrometer. Absolute calibration is required to calculate the excited state population densities required by the CR model codes. The optical emission is collected by a collimator and is coupled into a trifurcated fiber which delivers the light to three separate gratings and CCD arrays which are sensitive to three different bands (200–500 nm, 400–700 nm, and 600–870 nm). The second and third arrays are used for Ar II and Ar I spectra, respectively. The transmission coefficient through the clear Pyrex is assumed to be 1. The sensitivity of each channel was calibrated using an Optronic Laboratories Series 455 Integrating Sphere Calibration Standard to find the spectral radiance (W sr^{-1} cm^{-2} nm^{-1}) per photon count rate (count s^{-1}) as a function of the wavelength. The photon count rate is determined by summing the counts due to a given line and dividing by the integration time (from 3 to 900 ms, optimized for a given intensity). The absolute radiance L (in W sr^{-1} cm^{-2}) is found by multiplying the spectral radiance by the spectral width for each pixel in the vicinity of the line, which averages 0.18 nm. Though most lines of interest are completely resolvable, a number of lines overlap, either partially or fully. In cases of partial overlap, the ratio of peaks is used to apportion photon counts to each line. In cases of full overlap, the counts are apportioned using ratios determined by the relative intensities of each line as tabulated by NIST.[27] Once the absolute radiance of each line of interest is measured, the population densities (cm^{-3}) for each excited state k are given by

$$n_k = \frac{4\pi L}{A h \nu l}, \tag{2}$$

where A is the strength of the transition (s^{-1}), h is Planck's constant (J s), ν is the electromagnetic frequency of the transition (s^{-1}), and l is the optical path length (cm) which is taken as the entire 10 cm diameter of the chamber. It was found that saturation of some of the stronger lines under high rf power conditions occurred for the shortest integration time allowed by the Ocean Optics software (3 ms). To remedy this, a neutral density filter with an optical density of 0.5 (32% transmission at center wavelength) is placed in front of the collimator when necessary. The spectrometer was calibrated with and without the filter to account for its spectral response. Once determined spectroscopically, the excited state population densities can then be compared with densities predicted by the collisional-radiative codes to determine T_e and n_n.

T_e is determined with data computed using the Atomic Data and Analysis Structure (ADAS) CR model for argon ions.[18] ADAS is a set of computer codes developed to model radiation from both neutrals and ions for a variety of species. The code and technique we use to determine T_e with the ADAS model is based on and is very similar to that originally developed by Sciamma.[28] The Ar II ADAS CR model consists of a set of coupled differential equations for 35 level parents, which are groupings of excited states of singly ionized argon that share the same electronic configuration but differ in their total angular momentum. The population of each excited state is determined by solving these differential equations under a quasisteady-state approximation. The population n_i of each level parent k is given by

$$n_i(k) = R(k) n_e n_i(1) = R(k) n_e^2, \tag{3}$$

where $R(k)$ is the reduced population coefficient of level parent k, calculated by the ADAS code as a function of T_e and n_e using tabulated cross sections, and $n_i(1)$ is the ground state of Ar II. Quasineutrality $[n_i(1) = n_e]$ is assumed and ionization states higher than $Z=1$ are neglected. One can then determine T_e by finding the coefficients $R(k)$ that result in the computationally determined excited population densities $n_i(k)$ that match with the spectroscopically measured densities for the measured n_e. The coefficients over a range of T_e and n_e were calculated by Dr. W. L. Rowan for use by Sciamma using an atomic database developed by Loch.[29] The values for three level parents are used (for configurations $4p\ ^4P$, $4p\ ^4D$, and $4p\ ^2D$ corresponding to the ADAS level parent indices $k=13$, 14, and 15, respectively) which are associated with transitions for readily observed spectral lines (see Table I). Interpolation or extrapolation is used to find the population rates for values of n_e and T_e that lie between or beyond the values provided (1×10^{10} $cm^{-3} \leqslant n_e$

TABLE I. Emission lines used with the ADAS CR model.

Wavelength (nm)	Level Parent Index (k)	Configuration
433.1200	14	$4p\,^4D_{3/2}$
434.8064	14	$4p\,^4D_{7/2}$
437.9667	14	$4p\,^4D_{1/2}$
440.0097	13	$4p\,^4P_{3/2}$
440.0986	13	$4p\,^4P_{5/2}$
442.6001	14	$4p\,^4D_{5/2}$
443.0189	14	$4p\,^4D_{3/2}$
472.6868	15	$4p\,^2D_{3/2}$
473.5906	13	$4p\,^4P_{3/2}$
480.6020	13	$4p\,^4P_{5/2}$
484.7810	13	$4p\,^4P_{1/2}$
487.9864	15	$4p\,^2D_{5/2}$
496.5080	15	$4p\,^2D_{3/2}$
500.9334	13	$4p\,^4P_{5/2}$
506.2037	13	$4p\,^4P_{3/2}$

$\leqslant 2\times 10^{12}$ cm^{-3} and 0.5 eV$\leqslant T_e \leqslant$500 eV). As such, the code we use does not solve the CR equations but instead relies on precalculated values. Since the code requires input of both n_e and T_e it is necessary to know one of the quantities to determine the other. We have used the code to determine T_e with the experimentally determined n_e, though in principle the reverse can be performed. T_e measured using this method is a three-dimensional average so it is not possible to discern the ratio of the components in the parallel and perpendicular directions with respect to the magnetic field.

The Ar I CR model used to determine n_n was originally formulated by Vlček[17] and later expanded by Bogaert.[30] The code we use incorporating the Vlček model is based on and operationally identical to the code written by Keesee[6] and later adapted by Sciamma.[28] This model takes into account several mechanisms that contribute to the populations of the various excited Ar I states considered, including the excitation and de-excitation due to electron, ion, and neutral collisions, spontaneous radiative decay, radiative recombination, three-body recombination, and various metastable processes for the $4s[3/2]_2$ and $4s'[1/2]_0$ levels. The code is capable of calculating electron excitation, de-excitation, and ionization for arbitrary electron energy distribution functions, but a Maxwellian distribution is assumed here. Similar to the ADAS CR model, the Vlček model groups by level parent, and is made up of a set of 65 coupled differential equations. Unlike the method used to determine T_e, the Ar I CR code solves these equations for the various level populations rather than using precalculated tables. The code requires inputs of both n_e and T_e, the latter of which can be determined by the ADAS CR code, and assumes quasineutrality and singly ionized ions, as does the ADAS model. The neutral density is determined by finding the neutral density that, when entered into the code, results in level parent populations that correspond most closely with those measured spectroscopically. Readily observed lines allow computation of populations for four levels with configurations $4p'[3/2]_{1/2}$, $4p'[1/2]_1$, $4p[1/2]_0$, and $4p'[1/2]_0$ corresponding to level parent indices 8, 9, 10, and 11, respectively. (The primed and nonprimed configurations are for core quantum numbers $j_c=1/2$ and $j_c=3/2$, respectively.) Table II lists the emission lines used along with their level parent indices and electronic configurations.

TABLE II. Emission lines used with the Vlček CR model.

Wavelength (nm)	Level Parent Index (k)	Configuration
696.5431	9	$4p'[1/2]_1$
706.7218	8	$4p'[3/2]_2$
714.7042	8	$4p'[3/2]_1$
727.2936	9	$4p'[1/2]_1$
738.3980	8	$4p'[3/2]_2$
750.3869	11	$4p'[1/2]_0$
751.4652	10	$4p[1/2]_0$
772.4207	9	$4p'[1/2]_1$

The collisional-radiative spectroscopic diagnostics, as well as the 488 nm emission diagnostic, assume that no significant populations of doubly ionized or higher ionization states are present ($Z>1$). In order to verify this, optical spectra were measured to compare the emission levels for Ar II lines (found between 350 and 525 nm) and those for Ar III (found primarily in the UV band between 300 and 350 nm). The spectra were measured for the highest power level used (3 kW) and at the axial location where the ionization levels were the highest ($z=11$ cm). Accounting for UV transmission through the Pyrex and the calibrated instrument sensitivity in these two bands, the Ar II lines were found to be 50 times stronger than the Ar III lines on average, indicating that the doubly ionized population is indeed negligible.

III. RESULTS

A. Plasma density diagnostic comparison

In order to verify the accuracy of the various diagnostics, the plasma is formed with experimental parameters that allow multiple diagnostics to accurately measure the plasma density simultaneously. A comparison of axial plasma density (n_p) measurements is presented in Fig. 4, including n_e from interferometry, and n_p from the double probe and 488 nm emission, both calibrated with ADAS T_e measurements. (Thus the ADAS T_e diagnostic is implicitly cross-checked as well.) The experimental conditions are 800 W pulsed input rf power, 76 sccm flow rate (2.3 mTorr downstream end plate and 7.7 mTorr upstream end plate pressures), and 690 G magnetic field in the flat magnetic field configuration. The interferometer values are the peak on-axis values, derived from the line-averaged measurements using radial density profiles measured by the Langmuir probe. In the flat magnetic field configuration, the interferometer can only be used at $z=11$, 22, and 42 cm where there are gaps between the magnets. The double probe measurement is n_p at the center of the discharge which is found from the probe ion saturation current using T_e determined using the ADAS code

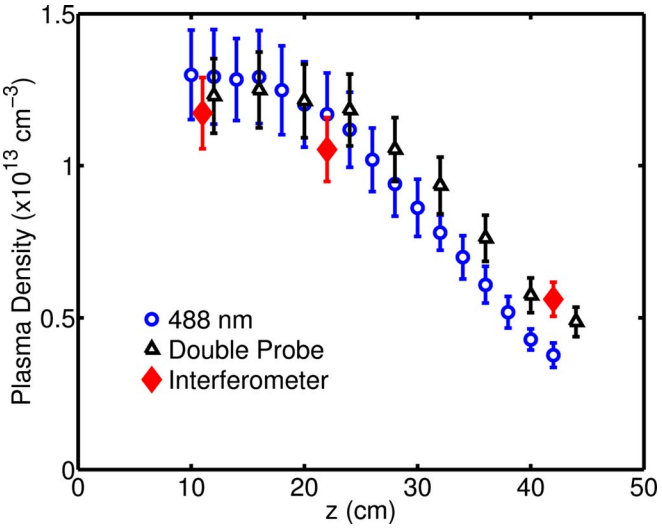

FIG. 4. (Color online) Comparison of plasma density measurements from interferometer (diamonds), double probe (triangles), and normalized square root of the 488 nm emission (circles). Error bars for the double probe and 488 nm emission represent shot-to-shot standard deviation and the noise level for the interferometer.

with the interferometer-measured n_e as an input. The 488 nm emission is also calibrated using this ADAS-computed T_e to determine the $\overline{\sigma_x v_e}$ factor as discussed in Sec. II. The square root of the temperature-calibrated 488 nm emission, which is proportional to the plasma density, is normalized for a best fit with the interferometer and double probe data points. The error bars in Fig. 4 for the 488 nm and double probe data represent the shot-to-shot standard deviation, while those for the interferometer data represent the noise level. Very good agreement between the three density measurements is observed along the axis of the experiment illustrating the high accuracy of the diagnostics.

The electron temperature was measured using the ADAS CR code at the three interferometer locations and was 2.8 ± 0.2 eV at both $z=11$ and 22 cm, and 2.6 ± 0.2 eV at 42 cm. A curve was fit to these data points for calibration of the double probe and 488 nm emission density measurements at other axial locations. While it is generally possible to extract T_e from the center of the double probe I-V curve, this portion of the curve is sensitive to rf probe potential oscillation effects and produces unreliable temperatures in high-density, near-source regions. However, very good T_e agreement between spectroscopy and double probe was found in the lower-density downstream region at $z=42$ cm, where rf effects are minimal. At this location the double probe indicated a T_e of 2.5 ± 0.2 eV and the ADAS-computed value at the same axial location was 2.6 ± 0.2 eV.

B. Experimental results

Figure 5 shows n_e from interferometry, T_e from the ADAS CR code, and n_n from the Vlček CR code upstream of the rf antenna at $z=-40$ and -25 cm as the input rf power is raised from 500 to 3000 W for an argon flow rate of 76 sccm and a nozzle configuration magnetic field of 1.04 kG. These quantities are line-averaged over the 10 cm

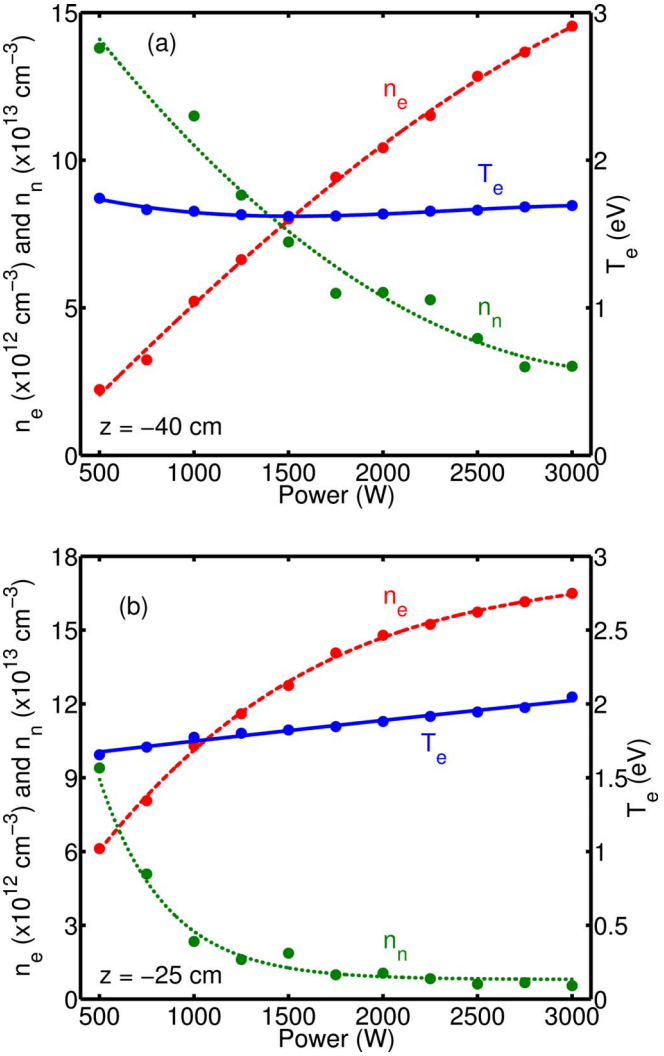

FIG. 5. (Color online) Upstream line-averaged electron density (dashed), neutral density (dotted), and electron temperature (solid) from interferometer, Vlček CR code, and ADAS CR code, respectively. Observation points are (a) $z=-40$ cm and (b) $z=-25$ cm with 76 sccm flow rate and 1.04 kG nozzle field. Note different vertical scales for n_e and n_n.

chamber diameter. At $z=-40$ cm [Fig. 5(a)], the electron density rises nearly linearly from 2.2×10^{12} cm^{-3} to 1.5×10^{13} cm^{-3} as the power is increased to 3 kW. Peak on-axis values are typically twice those of line-averaged values,[16] corresponding to a maximum n_e of 3×10^{13} cm^{-3} on axis. The neutral density simultaneously decreases from 1.4×10^{14} cm^{-3} to 3.0×10^{13} cm^{-3} as the ionization rate increases, corresponding to an increase in the fractional ionization from 2% to 33%. Note that n_n at the lowest power level (500 W) corresponds to a room-temperature (298 K) argon pressure of 4.3 mTorr, which is consistent with pressure measurements, lying between the plasma-off 76 sccm flow rate fill pressure measurements of 7.7 and 2.3 mTorr, at the upstream and downstream end plates, respectively. The electron temperature at $z=-40$ cm remains essentially constant over this power range, at 1.7 ± 0.1 eV.

The same set of plasma parameters is shown in Fig. 5(b) still upstream of the antenna at $z=-25$ cm. The electron density rises higher at this location, up to 1.6×10^{13} cm^{-3} at

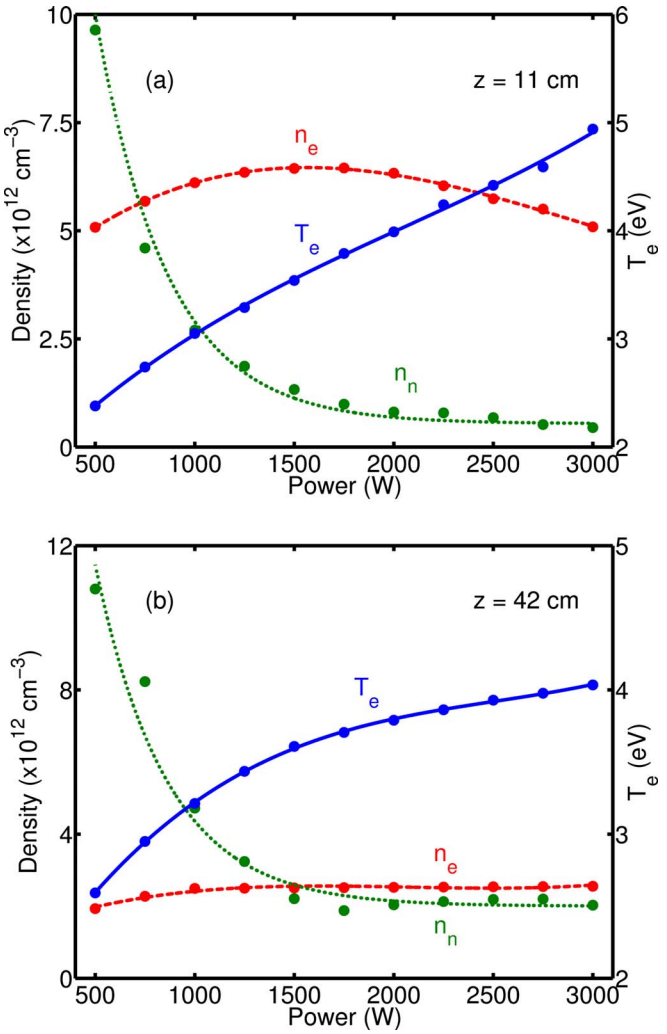

FIG. 6. (Color online) Downstream line-averaged electron density (dashed), neutral density (dotted), and electron temperature (solid) from interferometer, Vlček CR code, and ADAS CR code, respectively. Observation points are (a) $z=11$ cm and (b) $z=42$ cm with 76 sccm flow rate and 1.04 kG nozzle field.

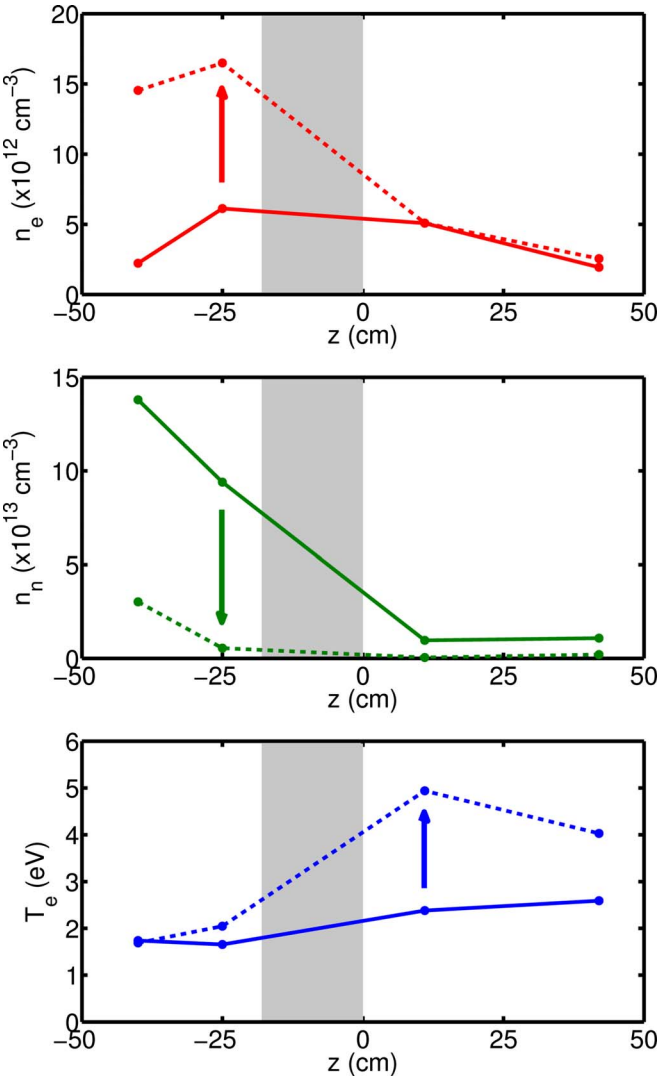

FIG. 7. (Color online) Variation of n_e, n_n, and T_e along the experimental axis for input powers of 500 W (solid) and 3 kW (dashed). Flow rate of 76 sccm with 1.04 kG nozzle configuration field. The shaded area indicates the extent of the antenna.

3000 W. The rate in the rise of n_e decreases as the power is increased to 3 kW in contrast to the more linear rise at $z=-40$ cm. T_e rises from 1.7 to 2.0 eV, in contrast to the nearly constant value of 1.7 eV measured upstream. The neutral density, as at $z=-40$ cm, drops with increasing power and ionization, but does so exponentially, decreasing from 9.4×10^{13} cm^{-3} at 500 W and ultimately leveling off at 8.1×10^{12} at 3 kW. This corresponds to a rise in fractional ionization from 6% to 75%.

A very different picture exists downstream of the antenna. Data for $z=11$ and 42 cm are shown in Figs. 6(a) and 6(b), respectively. At $z=11$ cm n_e rises from 5.1×10^{12} cm^{-3} to a maximum value of 6.5×10^{12} cm^{-3} at 1.5 kW, then decreases to 5.1×10^{12} cm^{-3} as the power is further increased to 3 kW. The neutral density falls exponentially over this power range from 9.6×10^{12} cm^{-3} to 5.4×10^{11} cm^{-3}. The corresponding line-averaged fractional ionization rises from 35% to 92%. Unlike the constant electron temperature seen upstream ($z=-40$ cm), at this downstream location T_e rises linearly from 2.4 to 4.9 eV.

Data taken farther downstream beyond the magnetic nozzle at $z=42$ cm is shown in Fig. 6(b). At this location n_e rises only slightly as the power is increased from 500 to 3000 W. T_e, similar to that observed at $z=11$ cm, rises from 2.6 to 4.0 eV. Unlike the value of T_e at $z=11$ cm however, the rise at $z=42$ cm is not linear, increasing at a slower rate as the power is increased. The neutral density at $z=42$ cm drops exponentially from 1.1×10^{13} cm^{-3} at 500 W to a steady value of $2.1\pm0.2\times10^{12}$ cm^{-3} from 1.5 to 3 kW, corresponding to a fractional ionization rising from 15% to 55 ± 2%. The behavior of n_n here is similar to that at $z=11$ cm, where n_n also levels out as the power is increased. The neutral density is higher however at $z=42$ cm, due to wall recombination in the expanding magnetic field lines beyond the nozzle.

To illustrate the variation of n_e, n_n, and T_e along the axis of the experiment, these quantities are shown as a function of axial position between $z=-40$ and 42 cm for the lowest and highest powers investigated (500 and 3000 W) in Fig. 7.

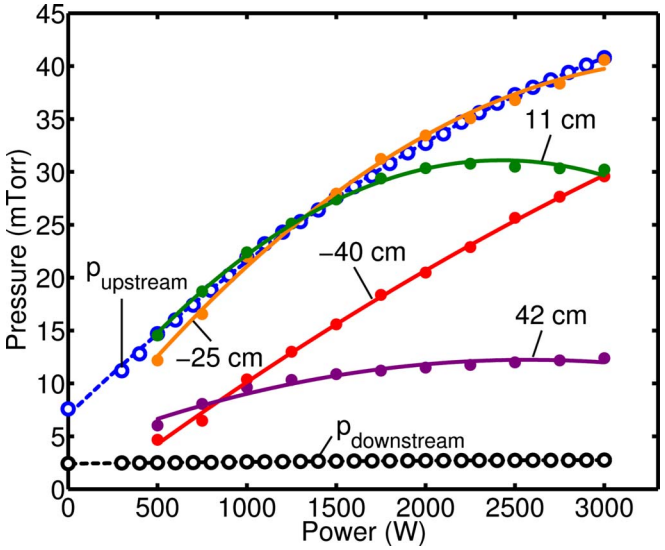

FIG. 8. (Color online) Total pressure measured at the upstream and downstream end plates (open circles, dashed lines) and electron pressure (closed circles, solid lines) at various axial positions as a function of input rf power for 1.04 kG source region field in the nozzle configuration and 76 sccm gas flow.

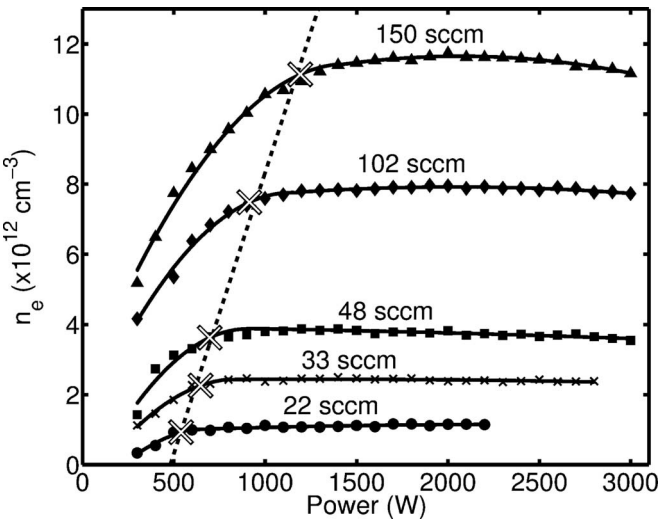

FIG. 9. Electron density as a function of input rf power for flow rates of 22 sccm (circles), 33 sccm (crosses), 48 sccm (squares), 102 sccm (diamonds), and 150 sccm (triangles). Nozzle configuration, 670 G source region field, observed at $z=11$ cm.

Arrows indicate the change in the quantities as the power is increased. Interferometer measurements were performed at $z=-74$ and 85 cm near the end plates, but the phase shifts at these locations were below the interferometer noise level for all pressures and powers investigated. This indicates that the electron density at these positions is below 1×10^{11} cm^{-3}, which corresponds to fractional ionization levels below 1%.

The electron pressure ($p_e=n_e k_B T_e$) at each axial location can be calculated using n_e from the interferometer and the spectroscopically measured T_e. The ion pressure can be neglected since $T_i \ll T_e$, therefore p_e can be considered as the total plasma pressure. Figure 8 shows the calculated p_e as a function of rf input power at each of the four interferometer locations, as well as the total pressures at the end plates measured by gauge. The measured plasma-off pressures are 7.7 mTorr at the upstream end plate and 2.3 mTorr at the downstream end plate. The upstream end plate pressure and p_e rise as the power is increased, while the downstream end plate pressure remains constant. The electron pressures at $z=-25$ and 11 cm closely correlate with the upstream end plate gauge pressure, except for high powers (above 1750 W) for which p_e at $z=11$ cm begins to diverge downward.

Figure 9 shows the line-averaged interferometer electron density at $z=11$ cm as a function of input rf power for a range of argon flow rates with a 690 G nozzle-configuration field. For a given flow rate, there is a power level at which a maximum n_e is attained. For flow rates 33 sccm and above, additional rf power actually leads to a small decrease in the local n_e. The density roll-off point for each pressure, defined as the intersection of straight-line fits of the rising and saturated regions, is indicated by $\times$ with a dashed line fit. Note that this roll-off point occurs at higher powers for higher fill pressures, showing that onset of density saturation occurs for higher powers as the fill pressure is increased.

Figure 10 illustrates the variation of n_e measured by the interferometer at $z=11$ cm for a flow rate of 76 sccm, as a function of rf input power and source-region nozzle-configuration magnetic field strength. For all magnetic field strengths, n_e reaches a maximum level and then decreases as the power is raised. This maximum value of n_e is a function of the magnetic field strength, and is highest for the highest field levels. Additionally, the rise and fall of n_e becomes more pronounced as the magnetic field is increased.

To illuminate the behavior of the plasma density in the vicinity of the magnetic nozzle, where the interferometer cannot be used due to obstruction by the electromagnets, 488 nm Ar II optical emission was measured along the axis of the experiment from $z=4$ to 42 cm for a range of rf power levels. Figure 11 shows the T_e corrected normalized square

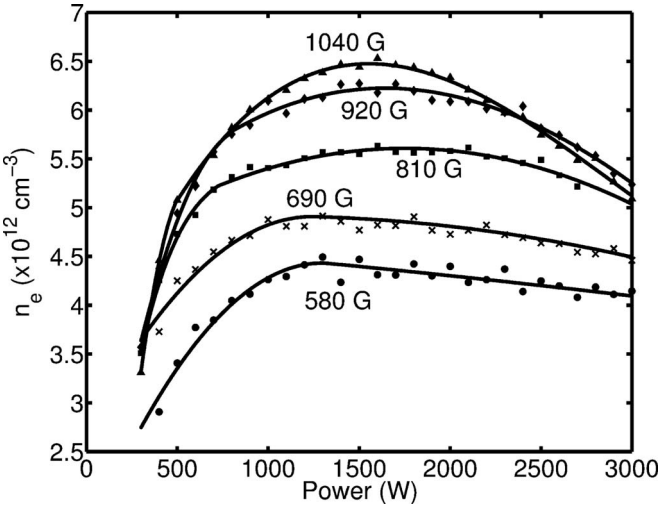

FIG. 10. Interferometer line-averaged n_e at $z=11$ cm as a function of input rf power for source region magnetic fields of 580 G (circles), 690 G (crosses), 810 G (squares), 920 G (diamonds), and 1040 G (triangles). Nozzle configuration with 76 sccm flow rate.

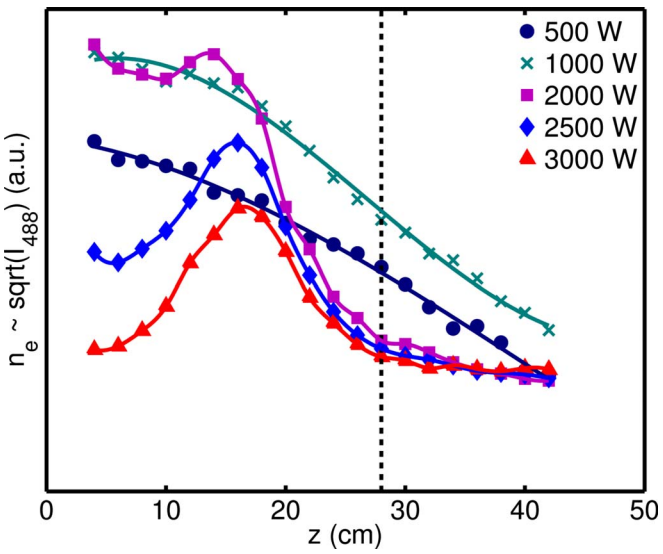

FIG. 11. (Color online) ADAS T_e-corrected square root of the 488 nm optical emission along the experimental axis for various powers. Nozzle configuration with 1.04 kG source region field and 76 sccm flow rate. The vertical dashed line denotes the position of the magnetic nozzle peak.

root of the 488 nm emission (proportional to the plasma density as discussed in Sec. II) as a function of axial position for the nozzle field configuration. The magnetic field strength is 1.04 kG, with a 76 sccm flow rate. Electron temperature measurements are only available at $z=11$ and 42 cm in this region, and a linear fit along the axis is used for calibration of the 488 nm emission in this region. For low powers (500 and 1000 W), the plasma density decreases monotonically moving axially downstream from the antenna source region. In contrast, for the highest power levels (2.5 and 3 kW), an apparent axial peak is seen at $z\approx 18$ cm. The overall density increases as the power is raised from 500 to 1000 W, but decreases as the power is raised from 2 to 3 kW, particularly in the region upstream of the nozzle peak ($z<28$ cm). These observations corroborate the rise and fall in the electron density observed at $z=11$ cm as the power is raised from 500 to 3000 W [see Fig. 6(a)].

IV. DISCUSSION

The plasma behavior as the input rf power is raised in the weakly depleted upstream region and the strongly depleted downstream region is fundamentally distinct. In the upstream region, increasing rf power contributes to increasing levels of ionization, but does not strongly heat the electrons (see Fig. 5), with T_e remaining nearly constant and below 2.0 eV. In the strongly depleted downstream region these patterns are essentially reversed (see Fig. 6). Here T_e rises linearly, from 2.4 eV to 4.9 eV at $z=11$ cm, while the electron density remains constrained, initially rising then falling as the power is increased. The onset of saturated plasma density associated with high neutral depletion in the downstream region is shown in Fig. 9, occurring between 500 and 1200 W as the flow rate is increased from 18 to 150 sccm.

The axial total pressure profile also varies between the upstream and downstream regions. The total pressure at any location is a sum of the contributions from electrons, ions, and neutrals and can be expressed as

$$p_{\text{tot}} = p_e + p_i + p_n = n_e k_B T_e + n_i k_B T_i + n_n k_B T_n, \tag{4}$$

where k_B is the Boltzmann constant. Near the end plates, neutral depletion rates are very low and p_{tot} is dominated by p_n. In the near-source downstream region, the neutral depletion is very high, and p_{tot} is dominated by p_e. In regions of intermediate levels of neutral depletion however, both p_e and p_n will contribute to p_{tot}.

Looking first at the region upstream of the antenna, we note that the level of ionization at $z=-25$ cm is substantial (up to 75%) so that $p_{\text{tot}}\approx p_e$. As shown in Fig. 8, p_e at this location is very close to the upstream end plate pressure at all powers between 500 and 3000 W. This indicates that a pressure balance exists between the incoming neutral gas and the plasma in the magnetized source region. Between these two locations, at $z=-40$ cm, the fractional ionization is lower (between 2% and 33%), so that p_n is a non-negligible component of p_{tot}. This neutral pressure (along with a small contribution from p_i) accounts for the difference between p_e at this location and the upstream end plate pressure in Fig. 8.

The difference in pressure at $z=-40$ cm can be used to estimate the local ion and neutral temperatures. Noting that T_e, n_e, n_i, n_n, and p_{tot} (taken as the pressure measured at the upstream end plate) are known, there remain only two unknowns in Eq. (4), T_n and T_i. We can estimate these temperatures under the assumption $T_n=T_i=T$. This shared temperature T can be expressed as

$$T = \frac{p_{\text{tot}} - n_e k_B T_e}{k_B (n_i + n_n)}. \tag{5}$$

This calculated temperature rises linearly from 0.05 eV to 0.2 eV as the power is increased from 500 to 3000 W. Since the ions are subjected both to the same heating mechanism that the neutrals experience (elastic collisions with electrons) as well as electromagnetic forces, the ion temperature is assumed to be larger than the neutral temperature. Therefore T can be considered an upper bound for T_n and a lower bound for T_i. The calculated temperature range is consistent with ion temperatures observed on other helicon experiments.[31]

Looking now at the pressure in the region downstream of the antenna, we see that p_e at $z=11$ cm is equal to the pressure in the upstream region for low power levels, but diverges downward as the power is increased to 3 kW (see Fig. 8). Farther downstream at $z=42$ cm, p_e is lower than the upstream pressure at all power levels. Unlike at $z=-40$ cm, n_n at these locations is very low, so that p_n is negligible and $p_{\text{tot}}\approx p_e$. At the downstream end plate the pressure is virtually unaffected by the power level, rising less than 1% when the plasma is turned on at 3 kW.

The total pressure as a function of axial position for 500 and 3000 W rf power, as well as when the plasma is off, is shown in Fig. 12. The end plate pressures are the direct gauge measurements ($p_{\text{tot}}\approx p_n$), while in the highly ionized

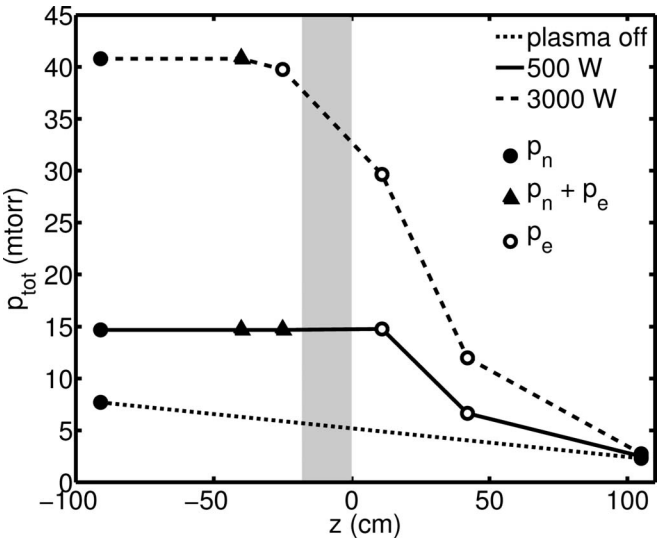

FIG. 12. Total pressure (p_{tot}) for 76 sccm over the entire axial extent of the chamber (z=−91 to 105 cm) for plasma off (dotted) as well as 500 W (solid) and 3000 W (dashed) rf power conditions. p_{tot} is assumed to be dominantly p_n (solid circles), p_e (open circles), and p_n+p_e (triangles) at various points. The shaded area indicates the antenna extent.

regions p_{tot} is taken as the measured p_e, and in the weakly ionized upstream locations p_{tot} is taken as the upstream end plate pressure to account for a non-negligible neutral pressure ($p_{tot} \approx p_n + p_e$). A straight-line fit is used to represent the plasma-off neutral pressure that falls monotonically towards the pump since the cross-sectional area of the chamber is constant. The ion pressure is assumed small at all locations ($T_i \ll T_e$). The upstream region exhibits a uniform pressure along the axis, while a pressure gradient is seen downstream, extending to the turbopump. The region of uniform pressure upstream is a consequence of the plasma in the magnetized source region exerting pressure against the incoming gas. The chamber is closed on the upstream end, leading to a balance of pressures in these two regions. The downstream end of the chamber, however, is effectively open, since particles escape through the turbopump. Instead of a uniform axial pressure profile, a pressure gradient exists in this portion of the chamber, extending from the source to the downstream end plate. This pressure gradient will accelerate the plasma in the positive z direction.

For all power levels there is a decrease in the plasma density along the axis between z=−25 and 11 cm. This is most profound at the highest power level (3 kW) when this decrease is by a factor of 3 (see Fig. 7). The lower plasma density in the downstream region compared to that seen upstream cannot be explained entirely by the fact that at these power levels, few neutrals pass through the antenna region to be locally ionized downstream. The large number of ions produced upstream from the antenna must be accounted for. These ions are either becoming depopulated through recombination as they travel towards the downstream region, or are becoming less dense as a result of axial acceleration. The intense ionization occurring in the antenna region dominates over losses due to wall recombination from radial flux as the particles flow through this region, evidenced by the profound drop in neutral density from z=−25 and 11 cm (see Fig. 7). Ruling out recombination, the decrease in plasma density must therefore be a consequence of axial plasma acceleration.

In steady state the total axial flux density of argon, both neutral and ionized, will be the same at every point along the system, and can be measured directly with the flow meter. At 76 sccm the total axial argon flux density through the 10 cm diameter chamber is $\Gamma_m=\Gamma_n+\Gamma_i=n_n v_n+n_i v_i=4.0\times10^{21}$ m^{-2} s^{-1}, where v_n and v_i are the axial neutral and ion velocities. Under the approximation that the argon flux in the highly ionized near-antenna region (z=25–11 cm) is dominated by ion flux ($\Gamma_m \approx \Gamma_i=n_i v_i$), and having ruled out significant recombination, the ion flux density through this region will be conserved. Ion flux conservation dictates that any decrease in ion density will be due to acceleration of the particles. Since the known axial argon flux at z=11 cm for high powers is primarily ions (92% ionization), we can neglect the small neutral flux and use the known n_i to estimate the ion flow velocity. The calculated ion velocity here is $v_i=\Gamma_i/n_i$=800 m/s, which is substantially higher than the neutral flow velocity at this location when the plasma is off, which lies between v_n=16 and 53 m/s measured at the upstream and downstream end plates, respectively (see Fig. 3). The ion sound speed for these conditions is $c_s=\sqrt{k_B T_e/m_i}$ =3.4 km/s (from T_e=4.9 eV), resulting in a Mach number $M=v_i/c_s$=0.24 at z=11 cm. Neglecting the neutral flux, at z=−25 cm the calculated ion velocity is v_i=250 m/s, with M=0.11 (T_e=2.0 eV). The lower fractional ionization there (75%) means that if v_n was a significant fraction of v_i, neutrals would contribute a non-negligible amount of the total argon flux. The calculated v_i at z=−25 cm is therefore an upper bound, meaning a lower bound for the acceleration of the ions through the antenna region at 3 kW is Δv_i =550 m/s. This plasma acceleration downstream of the antenna is due to the pressure gradient between the source region and the turbopump. Noting that the density and pressure gradients between z=−25 and 11 cm rise with increasing powers (see Figs. 7 and 12) this acceleration is directly proportional to the input rf power. The mobile electrons will be accelerated most strongly by this pressure gradient, and the resulting axially directed ambipolar[32] electric field will accelerate the ions so that $v_i > v_n$. As a consequence the ions passing through the slower-moving neutral population will experience a collisional drag that is proportional to n_n. The axial plasma velocity is thus also enhanced as a consequence of the reduced drag by the neutrals due to depletion.[13]

This neutral drag is a function of the ion-neutral collisional mean free path. For high-power operation where significant ionization leads to high levels of neutral depletion, there exist both collisional and collisionless regions in our helicon plasma with respect to electron-neutral and ion-neutral collisions. The mean free paths for ion-neutral (λ_{in}) and electron-neutral (λ_{en}) collisions vary significantly over the axial extent of the plasma chamber. The scattering cross section for ion-neutral collisions is $\sigma_{in}=5\times10^{-15}$ cm^2 for T_i near 0.1 eV,[33] which is typical for helicon sources.[31] The total electron-neutral scattering cross section is smaller, ranging from σ_{en}=3 to 8×10^{-16} cm^2 for the observed range of

$T_e = 1.7-4.9$ eV.[34] We therefore use $\lambda_{in} = 1/(n_n \sigma_{in})$ as a lower bound to evaluate collisionality, with corresponding λ_{en} values being an order of magnitude larger. The regions near both the upstream and downstream end plates exhibit high collisionality, where, due to extremely low ionization rates (less than 1%), λ_{in} is on the order of several cm. The ion mean free path in the near-source upstream region is somewhat longer due to a reduced neutral density there, but is still on the order of cm. In the highly ionized downstream near-source region at $z = 11$ cm, however, where the ionization level is above 90% at 3 kW, λ_{in} is on the order of several meters, so the plasma there can be considered collisionless. The collisionality of each region will determine the level of drag that the neutrals exert on the flowing ions.

Since the pressure gradient that drives the plasma acceleration is a function of the plasma density, and the plasma density is itself a function of the plasma acceleration (from flux conservation), these quantities are in a self-consistent equilibrium in steady state. Comparing the curves for 500 and 3000 W in Fig. 12, the pressure gradient region extends farther back towards the upstream side of the chamber as the power and neutral depletion levels are increased. This is a consequence of the reduction in collisional drag by the neutral particles, which determines the position at which the plasma particles begin to accelerate. This coincides with the transition zone between the upstream weakly depleted (collisional) region and the downstream strongly depleted (collisionless) region.

The accelerated plasma particles in the near-source region continue to flow downstream and ultimately encounter the magnetic nozzle. The peaked nozzle field results in a magnetic mirror with a ratio of 1.44 ($B_{0,\mathrm{peak}}/B_{0,\mathrm{source}}$). The number of particles that are reflected back towards the source is a function of the ratio of the components of the particle velocities perpendicular and parallel to the magnetic field lines. As the axial (parallel) plasma particle velocities are increased, the mirror effect that turns back electrons with high pitch angles (effectively an axially directed pressure acting against the plasma flow) will be reduced. The plasma density data in Figs. 9 and 10 show a rise and fall of the density in the region between the antenna and the magnetic nozzle peak as the power is increased. This is consistent with mirroring that is strong for low power levels and slower axial plasma particle velocities but is reduced for high axial velocities.

Typically in helicon experiments the plasma density and "blue core" optical emission are observed to be higher on the side of the rf antenna for which the wave propagates in the $+B_0$ direction,[16,20,25] where the helicon coupling efficiency is higher (in our experiment this is the downstream side of the antenna region). In this flowing experiment, in which the gas encounters the $-B_0$ region first, the efficient wave coupling in the downstream $+B_0$ region does not result in a higher plasma density there. Instead the density is higher on the upstream side for high powers, a consequence of the large neutral depletion rate in the near-upstream and antenna regions at high rf power levels. For low power levels, the upstream ionization rate on the $-B_0$ side of the antenna is insufficient to ionize the majority of neutrals, allowing a significant flux of neutrals to enter the antenna and $+B_0$ downstream regions to be efficiently ionized. For high power levels, the upstream ionization rate in the $-B_0$ region is very high, despite the lower rf wave coupling efficiency compared with the $+B_0$ region. Consequently the downstream region is essentially starved of neutrals and very little ionization occurs [see Fig. 6(a)]. Instead, the helicon wave energy coupled into the electrons is not lost through elastic neutral collisions and ionization, and instead causes a linear increase in T_e in the collisionless downstream region ($z = 11$ cm). For powers below 1 kW, the significantly stronger blue emission observed on the $+B_0$ side of the antenna is due to a higher T_e compared with the $-B_0$ side, rather than a higher plasma density.

V. CONCLUSION

Electron density, neutral density, and electron temperature have been measured in a flowing high-power argon helicon discharge using microwave interferometry and spectroscopy with collisional-radiative models. The detailed axial variation of these quantities has been presented. Regions of high and low neutral depletion (collisionless and collisional, respectively) have been identified in which fundamentally different behaviors are observed as the input rf power is increased. In the upstream collisional region, where the total pressure is axially uniform, the neutrals are not substantially depleted, and an increasing rf power contributes to increasing ionization and plasma density, with T_e remaining low and essentially constant. In the downstream region the pattern is reversed. Here profound neutral depletion causes n_e to remain constrained as the coupled rf power is increased, and the helicon wave power serves instead to heat the electrons, causing a linear increase in T_e. In contrast to the upstream region, a pressure gradient exists between the source and turbopump, whose axial extent is a function of the neutral depletion rate. The reduced downstream plasma density is evidence of a plasma flow accelerated by a pressure gradient with a reduced collisional drag from neutral particles and a reduced rate of plasma reflection by the magnetic nozzle.

ACKNOWLEDGMENTS

This research was supported by Air Force Office of Scientific Research Grant No. FA9550-06-1-0172.

[1] R. W. Boswell, Plasma Phys. Controlled Fusion **26**, 1147 (1984).
[2] J. Gilland, R. Breun, and N. Hershkowitz, Plasma Sources Sci. Technol. **7**, 416 (1998).
[3] S. Yun, K. Taylor, and G. R. Tynan, Phys. Plasmas **7**, 3448 (2000).
[4] D. G. Miljak and F. F. Chen, Plasma Sources Sci. Technol. **7**, 537 (1998).
[5] A. W. Degeling, T. E. Sheridan, and R. W. Boswell, Phys. Plasmas **6**, 1641 (1999).
[6] A. M. Keesee and E. E. Scime, Rev. Sci. Instrum. **77**, 10F304 (2006).
[7] A. Aanesland, L. Liard, G. Leray, J. Jolly, and P. Chabert, Appl. Phys. Lett. **91**, 121502 (2007).
[8] M. Shimada, G. R. Tynan, and R. Cattolica, Plasma Sources Sci. Technol. **16**, 193 (2007).
[9] M. J. Hartig and M. J. Kushner, Appl. Phys. Lett. **62**, 1594 (1993).
[10] M. D. Kilgore, H. M. Wu, and D. B. Graves, J. Vac. Sci. Technol. B **12**, 494 (1994).
[11] M. Shimada, G. R. Tynan, and R. Cattolica, J. Appl. Phys. **103**, 033304 (2008).

[12]S. Cho, Phys. Plasmas **6**, 359 (1999).
[13]A. Fruchtman, G. Makrinich, P. Chabert, and J. M. Rax, Phys. Rev. Lett. **95**, 115002 (2005).
[14]J.-L. Raimbault, L. Liard, J.-M. Rax, P. Chabert, A. Fruchtman, and G. Makrinich, Phys. Plasmas **14**, 013503 (2007).
[15]X. M. Guo, J. Scharer, Y. Mouzouris, and L. Louis, Phys. Plasmas **6**, 3400 (1999).
[16]S. M. Tysk, C. M. Denning, J. E. Scharer, and K. Akhtar, Phys. Plasmas **11**, 878 (2004).
[17]J. Vlček, J. Phys. D **22**, 623 (1989).
[18]ADAS website (http://www.adas.ac.uk/).
[19]X. Sun, C. Biloiu, R. Hardin, and E. E. Scime, Plasma Sources Sci. Technol. **13**, 359 (2004).
[20]P. Zhu and R. W. Boswell, Phys. Rev. Lett. **63**, 2805 (1989).
[21]S. Luo, C. M. Denning, and J. Scharer, J. Appl. Phys. **104**, 013301 (2008).
[22]K. Akhtar, J. E. Scharer, S. M. Tysk, and E. Kho, Rev. Sci. Instrum. **74**, 996 (2003).
[23]B. M. Annaratone, G. F. Counsell, H. Kawano, and J. E. Allen, Plasma Sources Sci. Technol. **1**, 232 (1992).
[24]N. Hershkowitz, in *Plasma Diagnostics*, edited by O. Auciello and D. L. Flamm (Academic, Boston, 1989), Vol. 1, p. 113.
[25]I. D. Sudit and F. F. Chen, Plasma Sources Sci. Technol. **5**, 43 (1996).
[26]A. I. Imre, A. I. Dashchenko, I. P. Zapesochnyi, and V. A. Kel'man, JETP Lett. **15**, 503 (1972).
[27]NIST Atomic Spectral Database (physics.nist.gov/PhysRefData/ASD).
[28]E. Sciamma, Ph.D. thesis, University of Texas at Austin, 2007.
[29]C. P. Balance, D. C. Griffin, M. S. Pindzola, and S. D. Loch, J. Phys. B **40**, 27 (2007).
[30]A. Bogaert, R. Gijbels, and J. Vlček, J. Appl. Phys. **84**, 121 (1998).
[31]R. F. Boivin and E. E. Scime, Rev. Sci. Instrum. **74**, 4352 (2003).
[32]M. A. Lieberman and A. J. Lichtenberg, *Principles of Plasma Discharges and Materials Processing* (Wiley, New York, 1994), pp. 131–132.
[33]A. V. Phelps, J. Appl. Phys. **76**, 747 (1994).
[34]A. Zecca, G. P. Karwasz, and R. S. Brusa, Riv. Nuovo Cimento **19**, 1 (1996).